Characterizing the performance of a POPS miniaturized optical particle counter when operated on a quadcopter drone

Zixia Liu[1], Martin Osborne[1,2], Karen Anderson[3], Jamie D. Shutler[3], Andy Wilson[2], Justin Langridge[2], Steve H.L. Yim[4,5,6,7], Hugh Coe[8], Suresh Babu[9], Sreedharan K. Satheesh[10], Paquita Zuidema[11], Tao Huang[4], Jack C.H. Cheng[4], Jim Haywood[1,2],

Affiliations:

[1]College of Engineering Mathematics, and Physical Sciences, University of Exeter, Exeter, Devon, UK

[2]Met Office, Fitzroy Road, Exeter, Devon, UK

[3]College of Life and Environmental Sciences, University of Exeter, Penryn, Cornwall, UK

[4]Department of Geography and Resource Management, The Chinese University of Hong Kong, Hong Kong, China

[5]Stanley Ho Big Data Decision Analytics Research Centre, The Chinese University of Hong Kong, Hong Kong, China

[6]Institute of Environment, Energy and Sustainability, The Chinese University of Hong Kong, Hong Kong, China

删除的内容: Jim Haywood[1,2],

删除的内容: .

[7]Asian School of the Environment, Nanyang Technological University, Singapore

[8]Department of Earth and Environmental Sciences, University of Manchester, Manchester, UK

[9]Space Physics Laboratory, Vikram Sarabhai Space Centre, Trivandrum, 695 022, India

[10]Centre for Atmospheric and Oceanic Sciences, Indian Institute of Science, Bangalore 560 012, India

[11]Rosenstiel School of Marine and Atmospheric Science, University of Miami, Miami, FL, USA

Correspondence to: J. Haywood (J.M.Haywood@exeter.ac.uk)

Abstract:

We first validate the performance of the Portable Optical Particle Spectrometer (POPS), a small light-weight and high sensitivity optical particle counter, against a reference scanning mobility particle sizer (SMPS) for a month-long deployment in an environment dominated by biomass burning aerosols. Subsequently, we examine any biases introduced by operating the POPS on a quadcopter drone, a DJI Matrice 200 V2. We report the root mean square difference (RMSD) and mean absolute difference (MAD) in particle number concentrations (PNCs) when mounted on the UAV and operating on the ground and when hovering at 10m. When windspeeds are low (less than 2.6 m/s), we find only modest differences in the RMSDs and MADs of 5% and 3% when operating at 10m altitude. When windspeeds are between 2.6 - 7.7m/s the RMSDs and MADs increase to 26.2% and 19.1%, respectively when operating at 10m altitude. No statistical difference in PNCs was detected when operating on the UAV in either

删除的内容: We report the root mean square difference (RMSD) and mean absolute difference (MAD) in particle number concentrations (PNCs) when operating on the ground and on the drone.

ascent or descent. We also find size distributions of aerosols in the accumulation mode (defined by diameter, d, where $0.1 \leq d \leq 1\mu m$) are relatively consistent between measurements at the surface and measurements at 10m altitude while differences in the coarse mode (here defined by $d > 1\mu m$) are universally larger. Our results suggest that the impact of the UAV rotors on the POPS PNCs are small at low windspeeds, but when operating under higher wind speed of up to 7.6m/s, larger discrepancies occur. In addition, it appears that the POPS measures sub-micron aerosol particles more accurately than super-micron aerosol particles when airborne on the UAV. These measurements lay the foundations for determining the magnitude of potential errors that might be introduced into measured aerosol particle size distributions and concentrations owing to the turbulence created by the rotors on the UAV.

1 Introduction

Atmospheric aerosols have a significant impact on Earth's climate as they affect the radiative balance of the Earth-Atmosphere system through the direct effect which refers to absorption and scattering of solar and terrestrial radiation, and the indirect effect which refers to the ability of aerosols to act as cloud condensation nuclei (CCN) (Haywood and Boucher, 2000; Boucher et al., 2013). Aerosol concentration and their intrinsic properties are spatially inhomogeneous owing to different emission sources, deposition processes, transports, and chemical reactions (e.g. Bellouin et al., 2005; Jiminez et al., 2009; Lack and Cappa, 2010; Atkinson et al., 2018; Yim et al., 2019; Yim et al., 2020).

删除的内容: acting

Among these properties, particle size distributions (PSDs) and number concentrations (PNCs) are of fundamental importance in determining the impact of aerosols on the atmospheric radiation budget via the aerosol direct and indirect effects. Based on observations of the size distributions of aerosols and aerosol refractive index, aerosol optical properties can be inferred (e.g. Atkinson et al., 2015). The size of aerosol particles is also of primary importance in cloud formation and precipitation (Yin et al., 2000; Liu et al., 2018; 2019a). As a result, in order to better understand the effect of aerosols on climate change, it is important to obtain a comprehensive and accurate characterization of the spatial distribution of aerosol concentration and properties. Aerosols can also impact atmospheric visibility (e.g. Horvath, 1981), air quality, and health (e.g. Li et al., 2003; Gu et al., 2016; 2018; 2020; Shi et al., 2019). In terms of scales, satellite observations (e.g. Bellouin et al., 2005) are able to provide near global coverage of aerosol optical depths, but are only able to provide bulk measurements of properties of the aerosol size distribution (e.g. fine mode fraction) and aerosol optical properties (e.g. aerosol absorption). Dedicated field sites (e.g. Zuidema et al., 2016, 2018) or dedicated sampling with aircraft instrumentation (e.g. Haywood et al., 2003a; 2020) are able to make much more detailed aerosol microphysical measurements, but are costly and aircraft cannot sample aerosols at low altitude in built-up urban regions owing to obvious safety concerns.

94 The atmospheric science community frequently utilizes optical particle counters (OPCs)
95 and Mie scattering theory for sizing individual aerosol particles (e.g. Burkhart et al.,
96 2010). Measurements of aerosols by small, unmanned aerial vehicles (UAVs) have
97 many advantages, such as low-cost, ease and cost of deployment, and ease of access to
98 inaccessible areas such as those close to urban conurbations. However, owing to
99 payload restrictions, UAVs require light-weight, minaturized OPCs. The Portable
100 Optical Particle Spectrometer (POPS) is an advanced and small low-cost, light-weight,
101 and high-sensitivity OPC, particularly designed for UAVs and balloon sondes (Gao et
102 al., 2013; 2016). In brief, the POPS samples particles by drawing air through an inlet
103 tube into an optical chamber, where it is illuminated by a 405nm laser. A sheath air
104 flow is used to focus the sample air into the centre of the laser beam, and the sample
105 flow is maintained at a near constant rate by an automatically regulated on-board pump.
106 Individual particle sizes are then inferred by comparing the recorded signal amplitudes
107 to scattering amplitudes calculated using Mie scattering theory.

108

109 The POPS has been carried by balloon sondes to study the vertical profile of the Asian
110 Tropopause Aerosol Layer (Yu et al., 2017), but quantitative data when deployed on a
111 quadcopter drone is very sparse. There have been some recent side-by-side tests of
112 miniaturized OPC instruments against more established instrumentation in controlled
113 environments. For example, Bezantakos et al. (2018) compared a newly developed
114 miniaturized OPC against a GRIMM OPC across a range of atmospheric conditions.
115 There have also been some very limited comparisons of miniaturized UAV-borne OPC

instrumentation against measurements on large atmospheric tower based instrumentation (Ahn, 2019). Neither of these studies used a POPS OPC. Questions about the impact of inlets, and aircraft boundary layer depths on aerosol measurements have been the subject of research on aerosol for decades (Huebert et al., 1990; Sanchez-Marroquin, 2019). A similar significant question related to deploying the POPS instrument on a quadcopter drone is whether the turbulence generated by the multiple rotors and the attitude adjustment required to maintain positional stability impact the measurements of the aerosol concentrations and size distributions, and if so, to what extent. Here we provide the first comprehensive documentation of the performance of the POPS on a multi-rotor UAV. We first investigated the performance of the POPS instrument in a closely controlled environment on the ground in a three-week comparison of the POPS against reference instruments. The POPS was deployed at the Atmospheric Radiation Measurements (ARM) mobile facility on Ascension Island during colocation of the Layered Atlantic Smoke Interaction with Clouds (LASIC; Zuidema et al., 2016) and CLoud-Aerosol-Radiation Interaction and Forcing: Year-2017 (CLARIFY-2017; Haywood et al., 2020) measurement campaigns. Subsequently, when back in the UK, we examined the influence of the drone rotors and variability in the drone attitude on the measured aerosol number concentration and size distribution. Section 2 presents the methodology used in the ground-based comparison on Ascension Island. Section 2 also provides details of the methodology adopted for the UAV-mounted flights in UK. Section 3 presents the results before conclusions and future work is presented in section 4.

删除的内容: the

2 Methods

2.1 A 20-day comparison

As part of the CLARIFY-2017 and LASIC campaign, the POPS was deployed at the ARM mobile site on Ascension Island located in the mid-Atlantic (7.96° S, 14.37° W) alongside an ARM operated SMPS. The time period for sampling for both instruments analyzed here was from 20th August to 9th September 2017 (20 days) continuously, during which time biomass burning aerosol originating from the African continent was frequently present (Zuidema et al., 2018; Haywood, 2020). The SMPS and the POPS were connected to a common aerosol inlet, however, in the case of the SMPS, the sample air was dried before it entered the instrument.

In common with other OPCs, the POPS size distributions are influenced by the refractive index assumed in the Mie calculations. The manufacturer (Handix Scientific) provides a calibration for the POPS using well-sized latex spheres with a refractive index (RI) of 1.615+0.001i at 405 nm. Prior to deployment to Ascension Island, the manufacturer's calibration of the POPS was adjusted through independent lab-based measurements using latex spheres at the UK's Facility for Airborne Atmospheric Research (FAAM, https://www.faam.ac.uk/). Mie calculations were made for the specific geometry of the POPS sampling chamber and laser poarisation. The calibration procedure and associated Mie calculations are detailed in Appendix A. Errors in the PSDs can be caused by sampling aerosols with a different refractive index to that of latex, particularly if they are significantly absorbing (e.g. Haywood et al., 2003). The

删除的内容: https://www.faam.ac.uk/)

independent lab-based calibration binning criteria were therefore adjusted assuming a RI of 1.54+0.027i at 405 nm, which is expected to be more representative of the biomass burning aerosol particles sampled at the ARM site during the CLARIFY deployment (Peers et al., 2019). In contrast to the optical sizing nature of the POPS, the SMPS that was operated by the ARM mobile Facility uses particle mobility subsequent to application of an electrostatic charge to size aerosol particles, a method which is independent of the refractive index (Ruzer and Harley, 2012).

In addition to applying fundamentally different methods to measure the size of particles, the POPS and SMPS cover different ranges of size distributions. The POPS measures particles within the diameter range from around 0.12 – 4.44μm (for RI = 1.54+0.027i at 405 nm), while the SMPS covers diameter ranging from around 0.01 to 0.45μm.

删除的内容：1.00

2.2 Drone-mounted POPS

The POPS required a carefully designed bespoke rig to fit it safely to a quadcopter drone for deployment. A DJI Matrice 200 V2 was used because it had a sufficient power and payload capacity to lift the POPS and even with the relatively high payload could offer reasonable endurance. The maximum flight time of the Matrice is 24 minutes with the maximum payload (1.45kg). University of Exeter and Met Office staff designed and fitted the POPS to the Matrice airframe (Figure 1). The POPS was installed at the bottom left of the fuselage and fixed on the customized 3-D printed landing gear. The inlet tube of the POPS (red oval in Figure 1) reached 20cm above the rotors. The

diameter of the inlet tube is 1mm and the sample flow rate is 3 cm^3/s, yielding a flow velocity of 3.8m/s. No attempt has been made to optimise this simple tube inlet for drone applications. The data were collected during 14 test flights in total from 18th December 2019 to 9th March 2020 to determine any impact of the rotors and attitude of the UAV on the data from the POPS. Each test flight was planned to be separated into three stages. During the first stage, the drone was on the ground with the rotors off for ten minutes (G_NR). In the second stage, the drone was on the ground with the rotors on for the next ten minutes (G_R). In the last stage the drone hovered at a fixed position and fixed altitude of ten meters above the surface for ten minutes (FLY). A summary of date and time of each test flight is given in Table 1. There are some deviations from the G_NR, G_R and FLY routines. T1 was a pre-test so there was no FLY. Additionally, due to high wind speeds and associated operational safety concerns, T9 and T13 had to reduce the test time of FLY to 7 minutes and 5 minutes, respectively. Three vertical profiles were made at the end of T10, T12, and T13, the details of which are provided in the caption of Table 1. The main purpose of profiling during T10, T12 and T13 was to investigate: 1) the stability in the POPS instrument when profiling up and down as this is likely to be a prime operating maneuver when flying scientific sorties in the future; 2) the performance of the POPS at different vertical ascent and descent rates; and 3) the accuracy of the POPS on the way up and way down which could conceivably be influenced by turbulent disturbance by the rotors, particularly on vertical descents when the aerosol inlet will be in the wake of the drone rotors. The test flights were all performed at the Streatham campus of the University of Exeter (50.73N, 3.53W), UK.

删除的内容: in Table 2

3 Results

3.1 Comparison of POPS data against data from LASIC/CLARIFY-2017.

Figure 2 shows the mean PSD measured by the POPS and SMPS for the 20-day period, respectively. Figure 2 represents the whole size range of the two instruments as well as the fitted PSD from measurements with a wing-mounted PCASP-100X mounted on the UK's Bae146 FAAM aircraft from a flight during CLARIFY-2017 (Peers et al., 2019), which has been shown to be representative of biomass burning aerosol during the wider CLARIFY-2017 measurement campaign (Wu et al., 2020). The POPS and SMPS were sampling at around 330m altitude ASL when at the LASIC site while the PCASP data from the CLARIFY campaign was collected from 1.9-7.3km ASL. That the POPS and SMPS show close overlap at the peak concentrations indicates that the counting statistics and the particle concentrations are similar between the instruments. The mean PSD measured by the POPS and SMPS shows reasonable agreement. Although the agreement is not as good as that demonstrated in other comparisons against SMPS instruments (e.g. Gao et al., 2016), any resulting errors in derived optical parameters are likely to be small provided the fit is reasonable over the 0.2-1.0 μm diameter range. Measurements of biomass burning aerosol over the Atlantic from the SAFARI-2000 campaign suggest that particles in this range contribute 93% of the scattering at 0.55μm (e.g. Table 1, Haywood et al., 2003). The PSD from the wing-borne PCASP-100X that was operated on the FAAM bears a close resemblance to the SMPS and POPS PSDs

删除的内容: to

except at particle sizes <0.2μm diameter and >0.7μm diameter. The discrepancy at particle sizes <0.2μm might be expected because the fits that are adopted by Haywood et al. (2003) and Peers et al. (2019) do not account for these small particles as they were developed with simplicity in mind for global general circulation models and for satellite retrievals respectively. Aerosols >0.7μm diameter that were observed by the POPS that were not present in the CLARIFY-2017 or SAFARI-2000 data may well be generated by dust generation from the arid surface of Ascension Island or by super-micron sea-salt from breaking waves. Taylor et al (2020) document the enhanced influence of the oceanic component of aerosols in the marine boundary layer, but this is not included in the CLARIFY-2017 or SAFARI-2000 log-normal fits which represent biomass burning aerosols only. Thus, the POPS instrument appears to provide a reasonably quantitative measure of optically active sub-micron biomass burning aerosols.

We also investigated the overall particle number concentration from the POPS, and examine the time series of the POPS measurements against some other key variables measured by the SMPS and other instrumentation at the ARM mobile facility. The upper panel of Figure 3a presents the 20-day intercomparison of the PNCs from the POPS and SMPS, and panel 3b shows the ratio of the two concentration measurements (POPS/SMPS). They show a good agreement between two instruments while the geometric mean diameter (GMD) the of the size distribution (Figure 3c) is above 0.12μm. Again, this illustrates that the POPS instrument measures accumulation mode aerosols reasonably accurately.

删除的内容:

We would expect biomass burning aerosols to be associated with an increase in carbon monoxide (CO; Haywood et al., 2003; Wu et al., 2020), and the concentrations measured by both the POPS and SMPS instruments are well correlated with the CO volume mixing ratio (as measured by a co-located CO analyzer – Figure 3d). The concentration data also show some correlation with the AODs as measured by a co-located AERONET Cimel sun-photometer (panel five, Figure 3), although this AOD is a column measurement rather than a point measurement so the influence of vertical profile will likely be important (e.g. Wu et al, 2020; Haywood et al, 2020).

删除的内容: mass

3.2 Test flight results

To determine the impact of rotors and drone attitude on the POPS, we focus on the comparison of PSD and PNC at three different stages: G_NR, G_R, and FLY. Table 1 summaries the mean PNC with standard deviation and the PNC percentage differences of each flight at different stages.

删除的内容: 3

3.2.1. Particle number concentration (PNC)

Compared with the mean PNC at G_NR, the mean PNC at G_R changed from -1% to 26%, and that at FLY changed from -1% to 63%, respectively. However, it is apparent that the differences of PNCs are much lower in the cases T1, T2, T6, T7, and T10 (less than 10%) in both stages. Figure 4 shows the probability density functions of PNC in each case. A constant bin width is utilized across the G_NR, G_R, and FLY PDFs of each flight. Unpaired two-sample t-tests were selected to detect the similarity of the PNCs at different stages as the t-test is the most popular parametric test for samples

删除的内容: The PNC at three stages of each case were separated into 15 bins.

following normal distribution for calculating the significance of a small sample size (De Winter, 2013). Here the PNC of G_NR was set as the control group, while that of G_R and FLY was set as the perturbation groups using the mean PNC at each stage every 30 seconds. Before the t-test, the Levene's test was performed which is an inferential statistic used to assess the equality of variances for a variable calculated for two or more groups (Levene, 1960). If the Levene's test cannot be passed, then the unequal variances t-test, which is a more conservative test, was be applied for the groups. The results (p value) of the t-test of each test flight are shown in Table 2.

For a significance level (α) set as 0.05, there are 5 test flights that passed the t test in both G_R and FLY stages (p value $\geq \alpha$), which means the PNC measured at G_R and FLY stage corresponded well with those measured at G_NR. These test numbers have been marked in bold italic font in Table 2. This result indicates that the impact of rotors and UAV attitude was not significant in these five cases. The other three cases (T8, T9, and T14) passed the t-test in the G_R stage, which are marked in italic font. The rest of test flights did not pass the t-test in either stage (marked in standard font). Through comparing the weather conditions, we find that the wind speed (Table 2) was relatively lower (0.5-2.6m/s) in the cases which pass the t-test at both stages. The wind speed in the Table 2 was provided from observations at Exeter airport with one-hour resolution. During the actual experiment, when the wind speed was high, visual observations by the drone pilot suggested that the drone swung from side to side in the air, causing increased variability in the pitch, yaw and altitude of the drone. As previously noted, on T9 and T13 the drone was forced to land early to ensure safety due to the high (>7

删除的内容: 4

删除的内容: in green and

删除的内容: 4

删除的内容: yellow and

删除的内容: red and

删除的内容: 4

删除的内容: 4

m/s) instantaneous wind speed.

To determine the impact of wind speed on PNC observed by the POPS, the cases are separated into 2 categories: low wind speed (w<2.6m/s) cases and high wind speed (2.6<w<7.7m/s) cases. The PNC root mean square differences (RMSD) and mean absolute differences (MAD) at G_R and FLY for all cases, low wind speed cases, and high wind speed cases are given in the Table 3. For all cases, PNC RMSD is less than 10.2% at G_R and less than 26.2% at FLY, and MAD is less than 7.8% at G_R and less than 19.1% at FLY. However, in the low wind cases, the RMSD and MAD fall to 2.4% and 2.3% at G_R, and 5% and 3% at FLY, respectively. In contrast, RMSD and MAD in the high wind cases increase to 12.6% and 10.9% at G_R, 31.4% and 26.3% at FLY, respectively. The variability in the pitch, yaw and altitude of the drone also impacted the orientation of the inlet of the POPS, which ideally should be perpendicular to the horizontal plane. Variations in the orientation of the inlet led to uncertainties in the sample flow rate. Table 4 shows mean sample flow rates with standard deviation at G_NR, G_R, and FLY for all cases. It is clear that for G_NR, the mean flow rates were constant across all tests and the standard deviation in the flow rates were very low. Comparing with G_NR, the mean sample flow rate and the standard deviation were almost unchanged with for G_R. This shows that operating the rotors alone didn't impact the sample flow rate. However, while the mean flow rate during FLY was identical to G_NR, the standard deviations increased during the FLY stage, particularly for the tests under high windspeeds. The mean value of the standard deviation for low

删除的内容: 5

删除的内容: 6

windspeed cases was 0.13, while for the high windspeed cases was 0.21 which may influence the accuracy of the POPS measurements.

3.2.2. The particle size distribution (PSD)

The PSDs at different stages and the mean PSDs ratios at G_R to G_NR and FLY to G_NR of each test flight are shown in Figure 5, which indicates that the cases with high similarity of PNCs (T1, T2, T6, T7, and T10) show agreement of the PSD. It also shows that the differences in sub-micron sizes are less than those in super-micron sizes at G_R and FLY. Therefore, the size distribution was separated into two modes, the accumulation mode ($0.1 \leq d \leq 1.0\mu m$) and the coarse mode ($d > 1.0\mu m$), to make a statistical analysis. Table 5 summarizes the PSDs percentage differences for two modes at G_R and FLY for each case. The PSDs RMSD and MAD for two modes at G_R and FLY for all cases, low wind cases, and high wind cases are given in Table 5. The percentage differences of the PSDs are less than 5.4% and 14.9% in low wind cases at the accumulation mode at G_R and FLY, respectively, while the variation in the PSD in the coarse mode is perhaps due to lower counting statistics at these sizes. In contrast PSDs of other cases show differences across the whole spectrum. Even in the accumulation mode, the differences of the PSDs between FLY and G_NR are up to 53.2% in the case T8. PSDs RMSD and MAD at the accumulation mode are 3.4% and 2.7% respectively at G_R in the low wind speed cases, but up to 12.9% and 11.1% at G_R in the high wind speed cases. These statistics again indicate that impacts of rotors and UAV attitude on the POPS measurements appear to be reduced in low wind speeds

删除的内容: It also shows that the differences of sub-micron sizes are less than those of super-micron sizes at G_R and FLY.

删除的内容: Table 7 summaries the PSDs percentage differences for two modes at G_R and FLY for each case.

删除的内容: 7

relative to higher wind speeds. PSD RMSDs and MADs at the coarse mode at G_R, and at the accumulation and coarse mode at FLY show the same result. Generally speaking, RMSDs and MADs indicate the impact of rotors and UAV attitude on the performance of the POPS in measuring the accumulation mode is lower than in measuring the coarse mode, for all cases. RMSDs in accumulation mode were 10.6% at G_R and 21.6% at FLY, while those in coarse mode were 32.2% and 49.5% for all cases. MADs showed the same trend as RMSDs. In the absence of independent multi-stage meteorological tower measurements (e.g. Ahn, 2019), it is difficult to assess how much of the variability in PNCs and PSDs is real, particularly when the drone is flying; there may be changes in PNC with altitude when compared to the surface PNCs owing to surface deposition. Alternatively, there may be trends in the particle concentrations that occur during the entire measurement period which spanned around 30 minutes duration. We determine trends in the G_NR and G_R statistics by determining the mean slope (particles / s) during the operating periods; only flights T4 and T6 show trends of greater than 0.1 particles per second (6 particles / minute) when averaged over both G_NR and G_R. Figure 4 shows that there is potentially an increase in the concentrations that are measured during T4, and that there is potentially a bi-modal number concentration measured during the G_NR sampling period for T6. As no trends are evident for the other flights, it can be inferred that there is no evidence of a systematic significant trend in atmospheric concentrations across all flights; any such trends are likely to be random. However, a potential solution to any concern would be to change the three stage sequence from G_NR, G_R, FLY to a five stage sequence of

删除的内容: Generally speaking, RMSDs and MADs indicate the impact of rotors and UAV attitude on the POPS operated in accumulation mode is lower than when in coarse mode, for all cases.

G_NR, G_R, FLY, G_R and G_NR. This sequence is suggested for future investigations.

3.2.3. The PNC during vertical profiles

Figure 6 presents the results of the vertical profile runs in T10, T12, and T13. The mean PNC with standard deviation on the way up and down are shown in Table 6. The PNC measured on the way up and way down show agreement. The best agreement is found in the high number concentration, low wind-speed case (T10), where the PNCs differ by an average of 0.5% between ascent and descent. Even in the high wind-speed cases when the variability might be expected to be largest owing to changes in the pitch and yaw of the drone, general agreement is found indicating that the vertical speed of the drone (which was approximately 0.5 to 1m/s) does not appear to have a significant impact. Note that the vertical profiles do indicate some variability in the vertical distribution with PNCs ranging from 1207±83 cm^{-3}, 69±14 cm^{-3}, and 90±11 cm^{-3} close to the surface to 1189±107 cm^{-3}, 55±11 cm^{-3}, and 72±15 cm^{-3} in ascent and 1395±83 cm^{-3}, 69±5 cm^{-3}, and 89±6 cm^{-3} close to the surface to 1201±101 cm^{-3}, 54±12 cm^{-3}, and 82±13 cm^{-3} in descent for flights T10, T12 and T13. The close to surface data were collected by the UAV-mounted POPS when the drone was 1-3 meters above the surface. This variability with height emphasizes the utility of small, instrumented UAVs for measuring PNCs and PSDs at low altitudes; measurements at such altitudes are impossible to probe with heavily equipped atmospheric research aircraft operating under standard aviation safety protocols.

删除的内容: 8

4 Discussion and conclusions

删除的内容: **Conclusions**

We have investigated the performance of POPS against a reference SMPS instrument while on the ground and also while operated on a quadcopter drone, DJI Matrice 200 V2, which is the first documented test of the performance of a POPS instrument on a UAV. The investigation includes two parts. The first is a long-term comparison between the POPS and other instruments during the CLARIFY-2017/LASIC and SAFARI-2000 project. The results show that the PNC measured by the POPS and that measured by the SMPS and PCASP indicate agreement in the optically important size range centred at around 0.3µm diameter. This indicates that despite its small size, when operating under controlled conditions on the ground, the POPS instrument performs relatively well. In the second part, we tested the impact of drone's rotors and, indirectly the attitude of the drone, on the performance of the POPS with a focus on two aspects, the PNC and PSD. We found RMSDs and MADs in PNC when operating a POPS on a small quad-copter to be less than 10.2% and 7.8%, respectively, when operating on the ground, and less than 26.2% and 19.1%, respectively, at 10m altitude under wind speed conditions of up to 7.7m/s. For wind speed of less than 2.6m/s, RMSDs and MADs fell to 2.4% and 2.3% when operating on the ground, and to 5% and 3% at 10m altitude. We also found no statistical difference in PNC when operating the UAV in either ascent or descent. As for the PSD, the accumulation mode aerosol size distributions were relatively invariant between measurements at the surface and measurements at 10m altitude with RMSD and MAD of less than 21.6% and 15.7%, respectively. The

differences between coarse mode super-micron aerosols measured at the surface and at 10m altitude were universally greater than those measured at the surface with a RMSD and MAD approaching 49.5% and 40.4%, but it is unclear whether this is due to loss of coarse mode aerosol particles to the surface or whether this is due to interference from the rotors. This impact appears to be most prevalent at the larger end of the POPS size range. While the increase in PNC from G_NR to G_R might be explained by generation or resuspension of aerosols from the surface by the rotors of the UAV, the increase from G_R to FLY is more difficult to attribute. The surface acts as a net sink in aerosols through dry deposition which could lead to an increase in PNC with altitude (e.g. Pellerin et al., 2017), but there are confounding factors from changes in the attitude of the drone and rapid changes in the attitude necessary for stabilizing the position of the UAV during FLY that could also influence the measurements. Indeed, there is evidence that fast adjustments to the attitude of the UAV increase the variability in the flow rate reported by the POPS sensor, particularly at higher windspeeds, where these corrections are larger. These results suggest that, when the wind-speed is modest, the POPS and UAV and very simple inlet combination examined here appears able to measure the aerosol PSD and PNC with reasonable fidelity, particularly for sub-micron aerosols.

In follow-up scientific observations, the POPS deployed on the quadcopter drone will be used to measure the aerosol properties in the atmospheric boundary layer (ABL) under polluted condition. Concentration of pollutants in the ABL frequently have a

strong correlation with atmospheric stability (Wang et al., 2013, Chambers et al., 2015) with stable conditions leading to the build-up of pollutants in the ABL. Wind-speeds are frequently low in stable conditions due to the lack of convection driven turbulence. Because these future measurements are likely under stable, non-turbulent conditions, wind-speed effects are not likely to cause significant problems. For other applications of the POPS on a quadcopter drone, such as the dispersion of pollutants in down-wind driven plumes, attention should be paid to the influence of the higher wind speeds.

Appendix A

POPS calibration

The calibration procedure used to adjust the POPS size bins for refractive index followed the general OPC calibration methodology described in Rosenberg et al. 2012 and Gao et al. 2016. By sampling a series of mono-disperse particles of known refractive index we compared the scattering amplitudes measured by the POPS to scattering amplitudes calculated using Mie theory. Scaling the Mie calculated amplitudes to match the measured scattering amplitudes results in a scaling factor that accounts for the POPS laser energy and detector efficiency. The scaling factor can then be used to convert Mie calculated scattering amplitudes for any refractive index to the arbitrary units of the POPS.

Calibration measurements

The calibration used NIST traceable polystyrene latex (PSL) spheres in 22 sizes,

ranging from 0.147µm to 3µm. The manufacturer's stated refractive index is 1.615-0.001i. An air source and a nebuliser cup were connected via rubber tubing to the POPS inlet and a few minutes of data collected for each of the 22 sizes of PSL sphere. The result was a histogram of POPS digitizer values for each size. We fitted normal distributions to these and took the mode and standard deviation as the POPS scattering value and associated error.

Polarised Mie scattering calculations for the POPS geometry

The Mie scattering calculations were made using the miepython library available from https://pypi.org/project/miepython/. We calculated POPS specific scattering amplitudes for spherical particles by integrating the scattering phase functions over only the POPS collection angles. Gao et al. 2016 describes the geometry of the POPS detection chamber and this is shown in Figure A1.

According to Bohren and Huffman 1983, for a homogeneous spherical particle illuminated by an electromagnetic plane wave $E_i = E_{\parallel i} + E_{\perp i}$, the scattered wave $E_s = E_{\parallel s} + E_{\perp s}$ as observed a constant distance from the particle can be written as:

$$\begin{bmatrix} E_{\parallel s} \\ E_{\perp s} \end{bmatrix} = constant \begin{bmatrix} S_2 & 0 \\ 0 & S_1 \end{bmatrix} \begin{bmatrix} E_{\parallel i} \\ E_{\perp i} \end{bmatrix} \quad \text{(A1)}$$

Where $E_{\parallel} + E_{\perp}$ are the components of the electric fields parallel and perpendicular to the scattering plane, and S_1 and S_2 are elements of the amplitude scattering matrix describing the angular distribution of the scattered light. According to Gao et al. 2016

the POPS laser diode is oriented such that the plane of polarisation of the laser is perpendicular to the scattering plane (so perpendicular to the plane of the page in fig. 1), and so $E_{\|i}$ = zero. As the diagonal elements of the amplitude scattering matrix are zero, $E_{\|s}$ is also zero, meaning that the scattered field contains no component parallel to the scattering plane. Therefore, the scattering amplitude for the POPS, σ_{pops}, is given by:

$$\sigma_{pops} = \frac{\pi {D_p}^2}{8} Q_{sca} \int_0^{2\pi} \int_0^{\pi} (|S_1|^2)\, F_{pops}(\theta, \varphi) \sin\theta \, d\theta d\varphi \quad \text{(A2)}$$

Where θ and φ are the zenith and azimuthal scattering angles respectively (we measure φ from horizontal - that is downwards from the plane perpendicular to the page in Figure A1). D_p is particle diameter, Q_{sca} is the Mie scattering efficiency factor and F_{pops} is a weighting function that accounts for the collection angles of the POPS. To construct the weighting function F_{pops} we find the combinations of θ and φ for which the phase function hits the collection mirror (F_{pops} = 1) and when it is outside of the mirror (F_{pops}= 0). From Figure A1 and the information given in Table A1, for 38°≤θ ≤142° and $\varphi = \pi/2$, the scattered beam hits the collection mirror a vertical distance q from the axis of the incident beam given by:

$$q = R \cos(90 - \theta) \quad \text{(A3)}$$

where

$$R = \frac{I_d \sin((90 - \theta) - \alpha)}{\sin(90 + \theta)} \quad \text{(A4)}$$

and

$$\alpha = \sin^{-1}\left(\frac{(l_d - d)\sin(90+\theta)}{l_d}\right) \quad \text{(A5)}$$

and using the lens equation

$$l_d = \frac{1}{\left[\frac{1}{fm} - \frac{1}{d}\right]} \quad \text{(A6)}$$

For a given value of θ, as the azimuthal angle φ rotates away from $\pi/2$, the distance q will shorten by a factor of cos (90 - φ), and when q is less than the distance h (the distance from the beam to the horizon of the mirror) the scattered beam will no longer hit the mirror. So finally, for 38°≤θ ≤142° we have:

F_{pops} = 1 where q cos (90 - φ) > h ; else F_{pops} = 0 (A7)

Results

The blue curve in Figure A2 is the result of using equations A1 and A7 and a refractive index of 1.615-0.001i for particle diameters 0.1µm to 4µm (as a sanity check, this curve is nearly identical in shape to that shown in Figure 6 of Gao et al. 2016). The scattering amplitudes measured during the calibration using PSL spheres are plotted in red. The vertical error bars are one standard deviation of the normal distribution. The Mie scattering curve has been scaled (using a least squares fit) to match the scattering amplitudes measured during the calibration using.

The black curve in Figure A2 is the result of using a biomass burning like refractive index of 1.54-0.27i in the Mie calculations. This curve has also been scaled using the same factor as the blue PSL sphere curve.

Bin boundaries for biomass burning like particles

For particle sizing, we used 16 bins logarithmically spaced along the scattering amplitude axis. We then used a monotonic fit to the scaled scattering amplitude curve for biomass burning to relate these bin boundaries to particle diameters, giving the bin boundaries as shown in Figure A3.

Acknowledgements: This work was supported by the Chinese University of Hong Kong – University of Exeter Joint Centre for ENvironmental SUstainability and REsilience (ENSURE) programme; ZL, MO, JH, KA, JS, TH, JC and SY would like to thank ENSURE for their financial support. JH, ZL and HC would also like to acknowledge NERC SWAAMI (South West Asian Aerosol Monsoon Interactions) grants NE/L013878/1 and NE/L013886/1 for partial funding of the research.

删除的内容:

References

Ahn, K-H, Aerosol 3D Profiling Using Compact Particle Measuring Instruments with Balloon and Drone System, *7th International Symposium on Ultrafine Particles, Air Quality and Climate (2019)*, DOI: 10.5445/IR/1000096749,

Albrecht, B. A. (1989). Aerosols, cloud microphysics, and fractional cloudiness. *Science*, *245*(4923), 1227-1230.

Atkinson, D. B., Pekour, M., Chand, D., Radney, J. G., Kolesar, K. R., Zhang, Q., Setyan, A., O'neill, N. T. & Cappa, C. D. 2018. Using spectral methods to obtain particle size information from optical data: applications to measurements from CARES 2010. Atmospheric Chemistry and Physics, 18, 5499-5514.

Atkinson, D. B., Radney, J. G., Lum, J., Kolesar, K. R., Cziczo, D. J., Pekour, M., Zhang, Q., Setyan, A., Zelenyuk, A. & Cappa, C. D. 2015. Aerosol optical hygroscopicity measurements during the 2010 CARES campaign. Atmospheric Chemistry and Physics, 15, 4045–4061.

Bezantakos, S., Schmidt-Ott, F., Biskos, G., 2018. Performance evaluation of the cost-effective and lightweight Alphasense optical particle counter for use onboard unmanned aerial vehicles. Aerosol Sci. Technol. 52, 385–392.

Bellouin, N., Boucher, O., Haywood, J., & Reddy, M. S. (2005). Global estimate of aerosol direct radiative forcing from satellite measurements. Nature, 438(7071), 1138-1141.

Boucher, O., D. Randall, P. Artaxo, C. Bretherton, G. Feingold, P. Forster, V.-M. Kerminen, Y. Kondo, H. Liao, U. Lohmann, P. Rasch, S.K. Satheesh, S. Sherwood, B. Stevens and X.Y. Zhang, 2013: Clouds and Aerosols. In: Climate Change 2013: The Physical Science Basis. Contribution of Working Group I to the Fifth Assessment Report of the Intergovernmental Panel on Climate Change [Stocker, T.F., D. Qin, G.-K. Plattner, M. Tignor, S.K. Allen, J. Boschung, A. Nauels, Y. Xia, V. Bex and P.M. Midgley (eds.)]. Cambridge University Press, Cambridge, United Kingdom and New York, NY, USA.

Burkart, J., Steiner, G., Reischl, G., Moshammer, H., Neuberger, M., & Hitzenberger, R. (2010). Characterizing the performance of two optical particle counters (Grimm OPC1. 108 and OPC1. 109) under urban aerosol conditions. Journal of Aerosol Science, 41(10), 953-962.

Chambers, S. D., Wang, F., Williams, A. G., Xiaodong, D., Zhang, H., Lonati, G., Crawford, J., Griffiths, A. D., Ianniello, A. & Allegrini, I. 2015. Quantifying the influences of atmospheric stability on air pollution in Lanzhou, China, using a radon-based stability monitor. Atmospheric Environment, 107, 233-243.

De Winter, J. C. 2013. Using the Student's t-test with extremely small sample sizes. Practical Assessment, Research, and Evaluation, 18, 10.

Gao, R., Perring, A., Thornberry, T., Rollins, A., Schwarz, J., Ciciora, S. & Fahey, D. 2013. A high-sensitivity low-cost optical particle counter design. Aerosol Science and Technology, 47, 137-145.

Gao, R., Telg, H., Mclaughlin, R., Ciciora, S., Watts, L., Richardson, M., Schwarz, J., Perring, A., Thornberry, T. & Rollins, A. 2016. A light-weight, high-sensitivity particle spectrometer for PM2. 5 aerosol measurements. Aerosol Science and Technology, 50, 88-99.

606 Gu Y. and Yim S.H.L. (2016). The air quality and health impacts of domestic trans-boundary
607 pollution in various regions of China. Environment International, 97, 117-124.
608 Gu Y., Wong T.W., Law S.C.K., Dong G.H., Ho K.F., Yang Y., Yim S.H.L. (2018). Impacts of
609 Sectoral Emissions in China and the Implications: Air Quality, Public Health, Crop
610 Production, and Economic Costs. Environmental Research Letters, 13, 8.
611 Gu Y., Zhang W., Yang Y., Wang C., Streets D.G., Yim S.H.L. (2020). Assessing outdoor air
612 quality and public health impact attributable to residential black carbon emissions in
613 rural China. Resources, Conservation and Recycling, 159, 104812.
614 Haywood, J., & Boucher, O. (2000). Estimates of the direct and indirect radiative forcing due to
615 tropospheric aerosols: A review. Reviews of geophysics, 38(4), 513-543.
616 Haywood, J., Francis, P., Dubovik, O., Glew, M. & Holben, B. 2003a. Comparison of aerosol
617 size distributions, radiative properties, and optical depths determined by aircraft
618 observations and Sun photometers during SAFARI 2000. Journal of Geophysical
619 Research: Atmospheres, 108.
620 Haywood, J. M., Osborne, S. R., Francis, P. N., Keil, A., Formenti, P., Andreae, M. O. & Kaye,
621 P. H. 2003b. The mean physical and optical properties of regional haze dominated by
622 biomass burning aerosol measured from the C-130 aircraft during SAFARI 2000.
623 Journal of Geophysical Research: Atmospheres, 108.
624 Haywood, J.M., S. J. Abel, P. Barrett, N. Bellouin, A. Blyth, K.N. Bower, M. Brooks, K. Carslaw,
625 H. Coe, M. Cotterell, I. Crawford, N. Davies, B. Dingley, P. Field, P. Formenti, H. Gordon,
626 M. de Graaf, R. Herbert, B. Johnson, A.C. Jones, F. Malavelle, D.G. Partridge, F. Peers,
627 J. Redemann, P. Stier, J. Taylor, R. Wood, H.H. Wu, P. Zuidema. Overview of the
628 CLoud-Aerosol-Radiation Interaction and Forcing: Year-2017 (CLARIFY-2017)
629 measurement campaign, acp-2020-729, Atmos Chem Phys Diss, 2020.
630 Horvath, H. (1981). Atmospheric visibility. Atmospheric Environment (1967), 15(10-11), 1785-
631 1796.
632 Huebert, B. J., Lee, G., & Warren, W. L. (1990). Airborne aerosol inlet passing efficiency
633 measurement. Journal of Geophysical Research: Atmospheres, 95(D10), 16369-
634 16381.
635 IPCC: Climate Change 2013: The Physical Science Basis. Contri- bution of Working Group I to
636 the Fifth Assessment Report of the Intergovernmental Panel on Climate Change,
637 Cambridge University Press, Cambridge, United Kingdom and New York, NY, USA, 2013.
638 Jimenez, J.L., Canagaratna, M.R., Donahue, N.M., Prevot, A.S.H., Zhang, Q., Kroll, J.H.,
639 DeCarlo, P.F., Allan, J.D., Coe, H., Ng, N.L. and Aiken, A.C., 2009. Evolution of organic
640 aerosols in the atmosphere. Science, 326(5959), pp.1525-1529.
641 Lack, D. & Cappa, C. 2010. Impact of brown and clear carbon on light absorption enhancement,
642 single scatter albedo and absorption wavelength dependence of black carbon.
643 Atmospheric Chemistry and Physics, 10, 4207.
644 Levene, H. 1960. Robust tests for equality of variances. Ingram Olkin, Harold Hotelling, et alia.
645 Contributions to Probability and Statistics: Essays in Honor of Harold Hotelling.
646 Stanford University, 278-292.
647 Li, N. Hao, M. Phalen, R. Hinds, W. and Nel, N. "Particulate air pollutants and asthma: a
648 paradigm for the role of oxidative stress in PM-induced adverse health effects." Clinical
649 immunology 109, no. 3 (2003): 250-265.

Liu Z., Ming Y., Zhao C., Lau N.C., Guo J., Bollasina M., Yim S.H.L. (2019a). Contribution of local and remote anthropogenic aerosols to a record-breaking torrential rainfall event in Guangdong Province, China. Atmospheric Chemistry and Physics, 20, 223-241.

Liu Z., Ming Y., Wang L., Bollasina M., Luo M., Lau N.C., Yim S.H.L. (2019b). A Model Investigation of Aerosol-Induced Changes in the East Asian Winter Monsoon. Geophysical Research Letters, 46(16), 10186-10195.

Liu Z., Yim S.H.L., Wang C., Lau N.C. (2018). The impact of the aerosol direct radiative forcing on deep convection and air quality in the Pearl River Delta region. *Geophysical Research Letters*, 45(9), 4410-4418.

Peers, F., Francis, P., Fox, C., Abel, S.J., Szpek, K., Cotterell, M.I., Davies, N.W., Langridge, J.M., Meyer, K.G., Platnick, S.E. and Haywood, J.M., 2019. Observation of absorbing aerosols above clouds over the south-east Atlantic Ocean from the geostationary satellite SEVIRI–Part 1: Method description and sensitivity. *Atmospheric Chemistry and Physics*, 19, 9595–9611, 2019 https://doi.org/10.5194/acp-19-9595-2019.

Pellerin, G., Maro, D., Damay, P., Gehin, E., Connan, O., Laguionie, P., Hébert, D., Solier, L., Boulaud, D., Lamaud, E. and Charrier, X., 2017. Aerosol particle dry deposition velocity above natural surfaces: quantification according to the particles diameter. *Journal of Aerosol Science*, *114*, pp.107-117.

Ruzer, L. S. & Harley, N. H. 2012. Aerosols handbook: measurement, dosimetry, and health effects, CRC press.

Sang-Nourpour, N., & Olfert, J. S. (2019). Calibration of optical particle counters with an aerodynamic aerosol classifier. *Journal of Aerosol Science*, 138, 105452.

Sanchez-Marroquin, A., Hedges, D. H. P., Hiscock, M., Parker, S. T., Rosenberg, P. D., Trembath, J., Walshaw, R., Burke, I. T., McQuaid, J. B., and Murray, B. J.: Characterisation of the filter inlet system on the FAAM BAe-146 research aircraft and its use for size-resolved aerosol composition measurements, Atmos. Meas. Tech., 12, 5741–5763, https://doi.org/10.5194/amt-12-5741-2019, 2019.

Shi C., Nduka I.C., Yang Y., Huang Y., Yao R., Zhang H., He B., Xie C., Wang Z., Yim S.H.L. (2019). Characteristics and Meteorological Mechanisms of Transboundary Air Pollution in A Persistent Heavy PM2.5 Pollution Episode in Central-East China. *Atmospheric Environment*, 223, 117239.

Taylor, J. W., Wu, H., Szpek, K., Bower, K., Crawford, I., Flynn, M. J., Williams, P. I., Dorsey, J., Langridge, J. M., Cotterell, M. I., Fox, C., Davies, N. W., Haywood, J. M., and Coe, H.: Absorption closure in highly aged biomass burning smoke, *Atmospheric Chemistry and Physics*, 20, 11201–11221, https://doi.org/10.5194/acp-20-11201-2020, 2020.

Twomey, S. (1977). The influence of pollution on the shortwave albedo of clouds. *Journal of the atmospheric sciences*, 34(7), 1149-1152.

Wang, F., Zang, H., Ancora, M. & Deng, X. 2013. Measurement of atmospheric stability index by monitoring radon natural radioactivity. *China Environmental Science*, 33, 594-598.

Wu, H., J.W. Taylor, K. Szpek, P.I. Williams, M. Flynn, J. Langridge, J.D. Allan, J. Pitt, S. Abel, J. Haywood, H. Coe, Vertical and temporal variability of the properties of transported biomass burning aerosol over the southeast Atlantic during CLARIFY-2017, *ACPD*..

Yim S.H.L., Gu Y., Shapiro M., Stephens B. (2019). Air quality and acid deposition impacts of local emissions and transboundary air pollution in Japan and South Korea. *Atmospheric*

带格式的: 正文, 缩进: 左侧: 0 厘米, 悬挂缩进: 3.5 字符, 首行缩进: -3.5 字符

带格式的: 字体: 10 磅, 字体颜色: 红色, 检查拼写和语法, 图案: 清除 (白色)

Chemistry and Physics, 19, 13309-13323.

Yim S.H.L. (2020). Development of a 3D Real-Time Atmospheric Monitoring System (3DREAMS) Using Doppler LiDARs and Applications for Long-Term Analysis and Hot-and-Polluted Episodes. *Remote Sensing* 12 (6), 1036.

Yin, Y., Levin, Z., Reisin, T. G. & Tzivion, S. 2000. The effects of giant cloud condensation nuclei on the development of precipitation in convective clouds—A numerical study. *Atmospheric Research*, 53, 91-116.

Yu, P., Rosenlof, K. H., Liu, S., Telg, H., Thornberry, T. D., Rollins, A. W., Portmann, R. W., Bai, Z., Ray, E. A. & Duan, Y. 2017. Efficient transport of tropospheric aerosol into the stratosphere via the Asian summer monsoon anticyclone. *Proceedings of the National Academy of Sciences*, 114, 6972-6977.

Zuidema, P., Sedlacek III, A.J., Flynn, C., Springston, S., Delgadillo, R., Zhang, J., Aiken, A.C., Koontz, A. and Muradyan, P., 2018. The Ascension Island boundary layer in the remote southeast Atlantic is often smoky. *Geophysical Research Letters*, 45(9), pp.4456-4465.

Zuidema, P., Redemann, J., Haywood, J., Wood, R., Piketh, S., Hipondoka, M. and Formenti, P., 2016. Smoke and clouds above the southeast Atlantic: Upcoming field campaigns probe absorbing aerosol's impact on climate. *Bulletin of the American Meteorological Society*, 97(7), pp.1131-1135.

删除的内容:

Figure 1. The DJI Matrice 200 V2 with the POPS (white box at the left bottom of the fuselage). The red oval shows the inlet tube leading to the POPS.

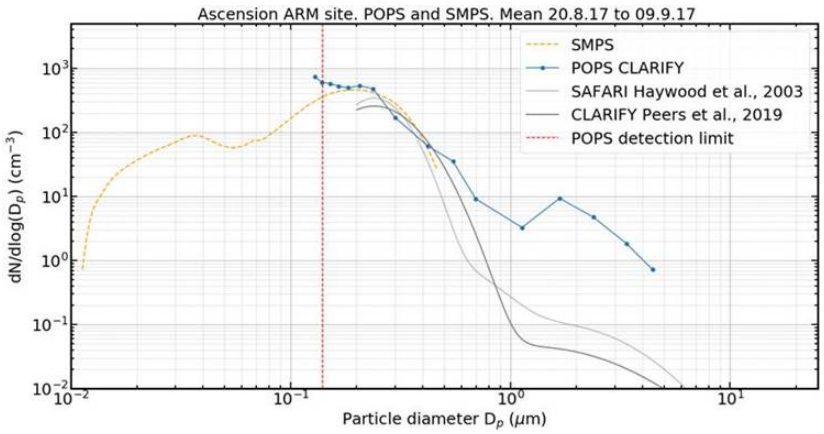

Figure 2. PSDs from POPS, SMPS, and data fitted to a wing-mounted PCASP from CLARIFY-2017 and SAFARI-2000. POPS and SMPS data were collected at the ARM mobile site on Ascension Island from 20th of August to 9th of September 2017.The PCASP data from CLARIFY were collected from a flight on 4th of September 2017 (Peers et al., 2019). The PCASP data from SAFARI-2000 represent a mean from 11 flights performed off the coast of Namibia (Haywood et al., 2003). Note that the CLARIFY-210 and SAFARAI-2000 PCASP distributions are 'scaled' to the SMPS size distribution to aid comparison. The POPS and SMPS values are not scaled.

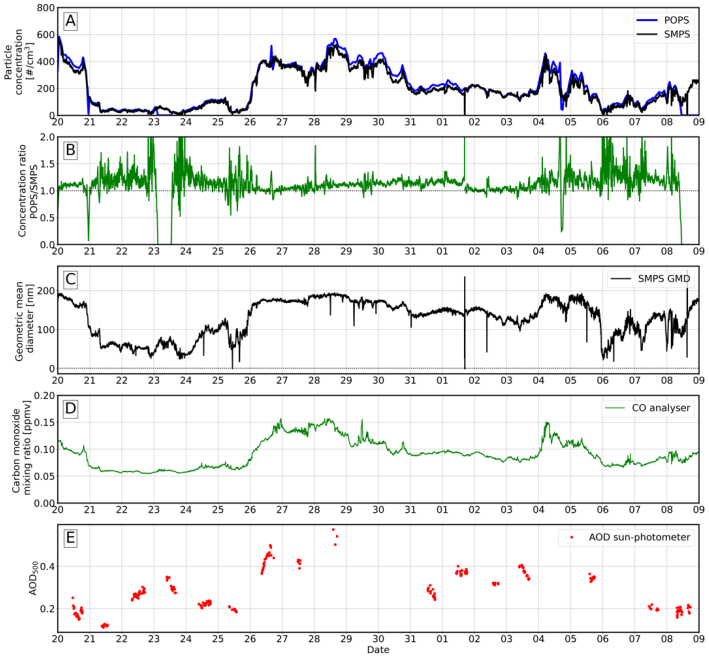

Figure 3. From top to bottom. (a) Time series of SMPS and POPS particle concentrations in the diameter range 120 – 450 nm measured during the LASIC/CLARIFY-2017 campaign. (b) Ratio of the POPS to SMPS concentrations shown in (a). (c) Geometric mean diameter from SMPS. (d) Carbon monoxide mixing ratio from Los Gatos Research CO analyser, and (e) AOD from Cimel sun- photometer.

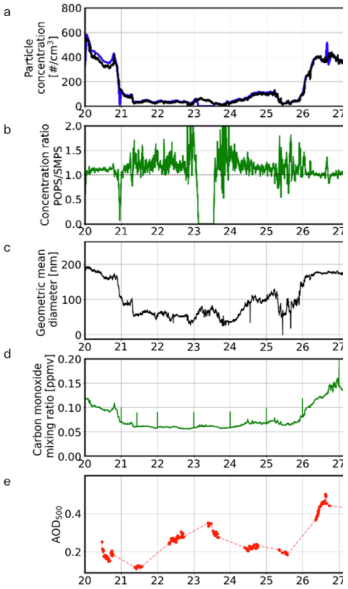

删除的内容:

删除的内容: From top to bottom. (a) SMPS and POPS total particle concentration. The number distribution is calculated over the range of bins that overlap between the two instruments (approximately 120 - 450nm diameter). (b) Ratio of POPS to SMPS total particle concentration derived from (a). (c) Geometric mean diameter from SMPS. (d) Carbon monoxide mixing ratio from Los Gatos Research CO analyser, and (e) AOD from Cimel sun- photometer. Spikes in the CO data occur at the beginning of each day when the instrument is in calibration mode.

删除的内容:

带格式的: 缩进: 左侧: 0 厘米, 首行缩进: 0 字符

删除的内容:

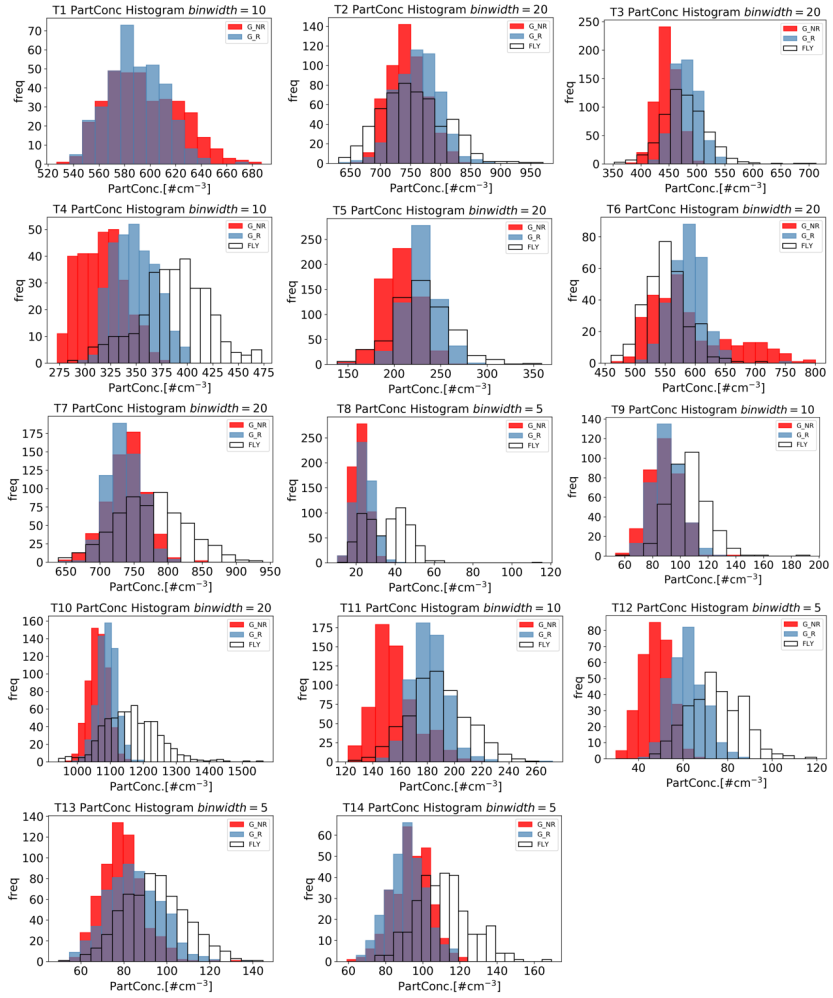

Figure 4. Probability density functions (PDFs) of PNCs in each case. A constant bin width is utilized across the G_NR, G_R, and FLY PDFs of each flight.

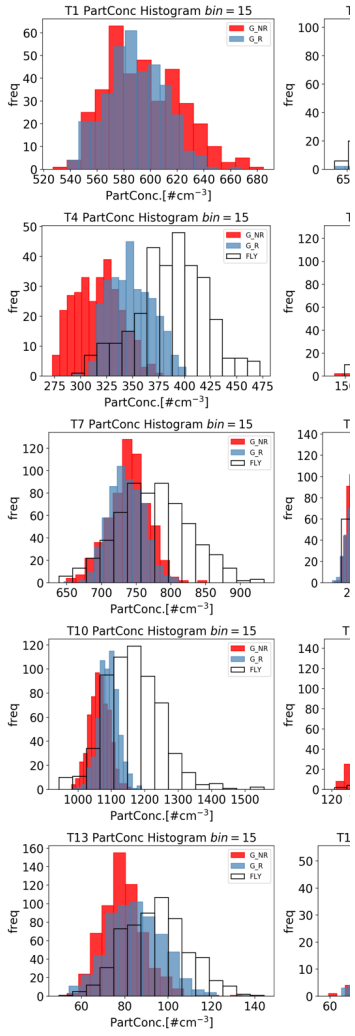

删除的内容:

删除的内容: Probability density functions of PNCs in each case. The bin number was set to 15 for all stages. Red represents the G_NR, blue represents G_R, and white represents FLY.

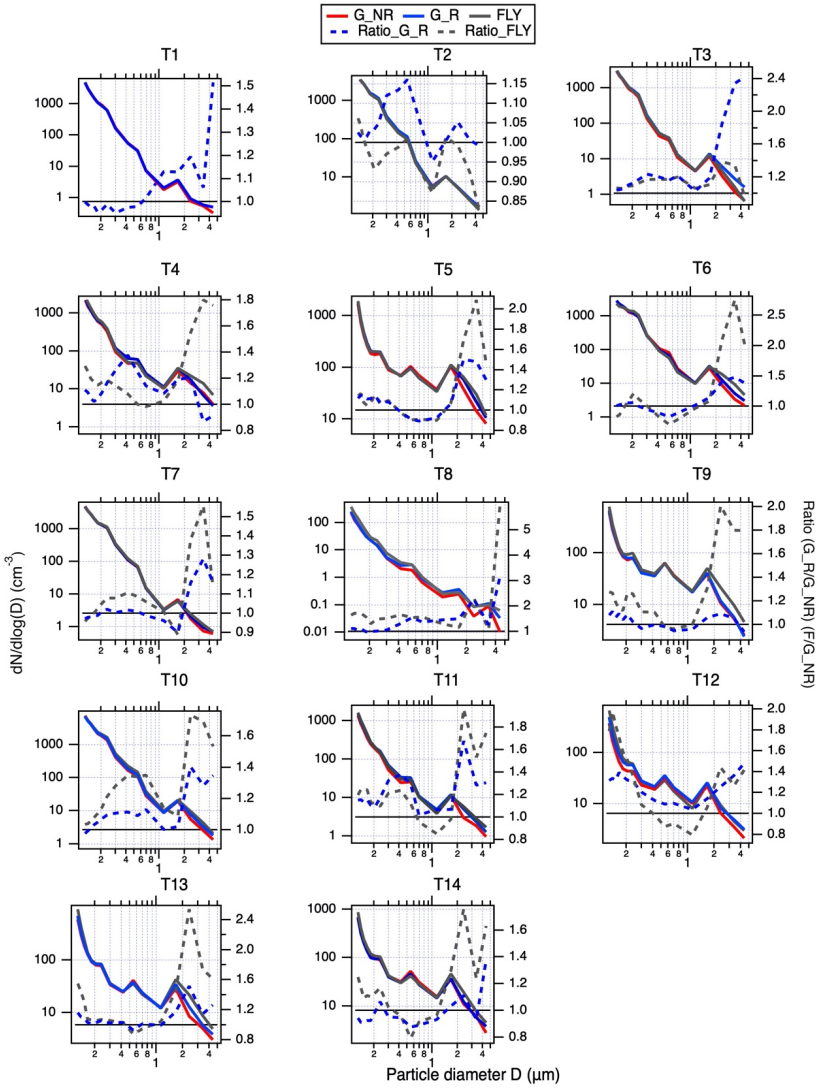

Figure 5. Particle size distribution at three stages: the drone on the ground with rotors off (G_NR) (red line), on the ground with rotors on (G_R) (blue line) and flying at 10m (FLY) (grey line), in each POPS test. The ratios of the PSD at G_R to G_NR (blue dash line) and at FLY to G_NR (grey dash line) of each flight are given in each plot.

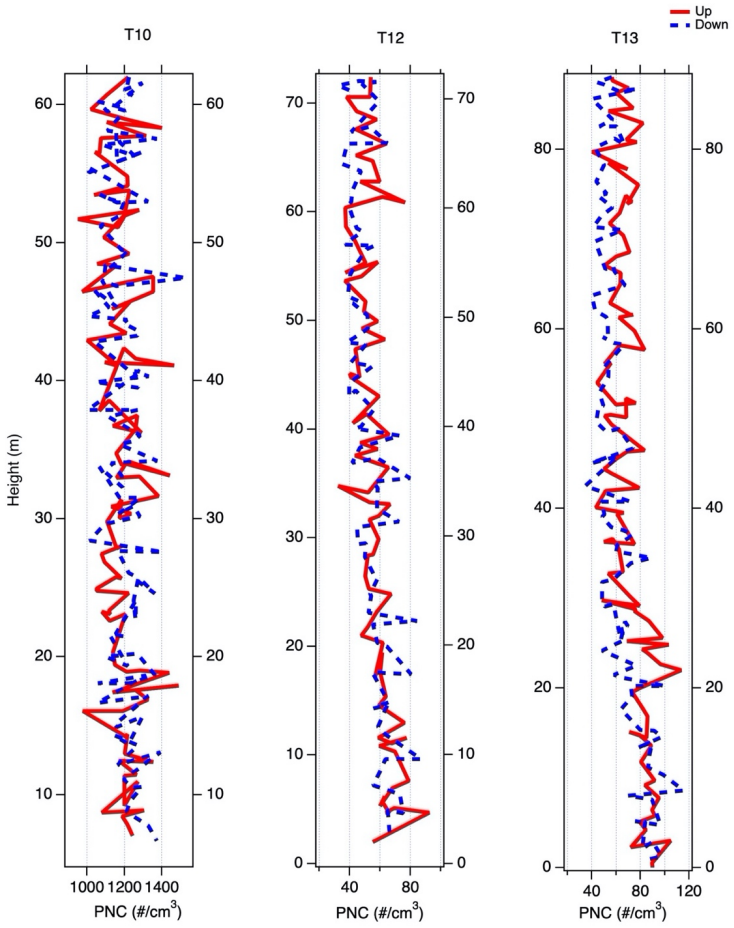

Figure 6. Vertical profiles of the particle number concentration in the profile runs of T10, T12, and T13. The red line shows the observed concentration in the way up and the blue dash line shows that in the way down, respectively.

删除的内容:

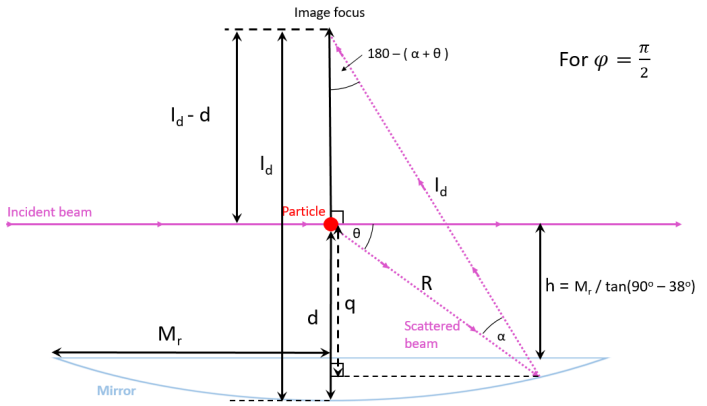

Figure A1. Geometry of POPS optical chamber. Values for the fixed parameters are listed in Table A1.

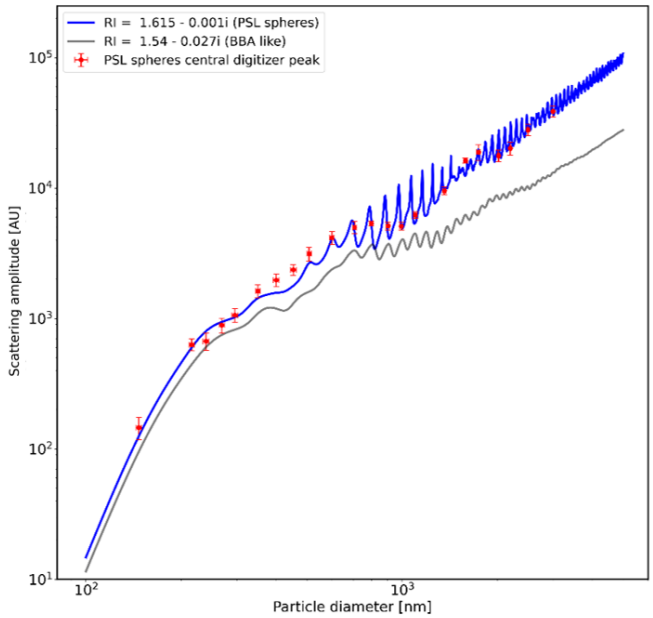

Figure A2. POPS scattering amplitudes for particles from 0.1μm to 4μm. Calculations for the blue curve used the refractive index for PSL spheres and for the black curve a refractive index for biomass burning particles. The red points are the real scattering amplitudes measured during the calibration with PSL spheres. Both the blue and black curves have been scaled using the same scaling factor.

带格式的: 居中

带格式的: 居中

带格式的: 两端对齐

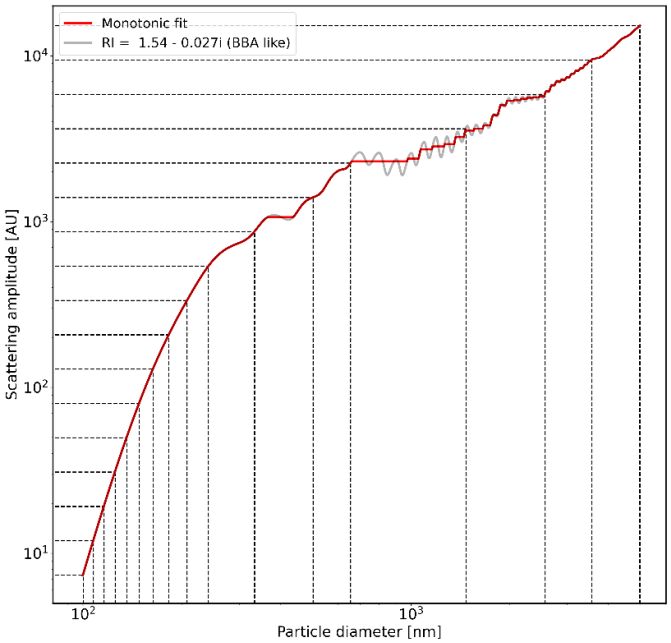

Figure A3. 16 bin boundaries logarithmically spaced in terms of peak value related to particle diameter using the scaled biomass burning curve from figure A2. The red line is a monotonically increasing fit.

带格式的: 居中

删除的内容: ↵
Date
... [1]

	Date & Time	Time	Particle Number Concentrations (PNCs) (cm^{-3})			Percentage Difference (%)	
			G_NR	G_R	FLY	G_R	FLY
T1	18/Nov/2019	16:07-16:30	597±30	587±22	n/a	-1.7	n/a
T2	19/Nov/2019	17:00-17:35	741±52	767±35	742±31	3.5	0.1
T3	20/Nov/2019	14:20-15:10	442±48	479±23	478±40	8.4	8.1
T4	25/Nov/2019	10:36-11:15	317±36	349±21	385±30	10.1	21.5
T5	26/Nov/2019	15:21-16:00	207±19	228±18	230±31	10.1	11.1
T6	28/Nov/2019	11:08-11:46	567±50	580±30	561±41	2.3	-1.1
T7	2/Dec/2019	11:45-12:31	753±30	745±24	760±55	-1.1	0.9
T8	30/Jan/2020	11:49-12:34	22±4	24±5	36±11	9.1	63.6
T9	4/Feb/2020	10:41-11:15	87±11	91±11	105±19	4.6	20.7
T10*	7/Feb/2020	11:57-12:44	1063±29	1092±29	1169±84	2.7	9.9
T11	12/Feb/2020	16:35-17:26	156±16	181±13	187±21	16.0	19.9
T12*	26/Feb/2020	14:36-17:27	50±7	63±9	74±11	26	48
T13*	3/Mar/2020	11:24-12:06	79±10	86±13	102±13	8.9	29.1
T14	9/March/2020	11:55-12:28	95±12	90±10	108±14	-5.3	13.7

Table 1. Summary of the PNCs of each test flight at three stages. n/a = not applicable. The numbers denoted by ±x represent the standard deviation in the PNCs during the measurement time period.* indicates that profiles were also performed as documented here. T10: 5-60 m at 0.5 m s^{-1}; T12: 5-70 m at 1.0 m s^{-1}; T13: 2-90 m at 1.0 m s^{-1}.

删除的内容: **Table 2.** Summary of the initial and end heights and vertical speed of each vertical profile.

删除的内容: **Table 3.** Summary of the PNCs of each test flight at three stages. n/a = not applicable. The numbers denoted by ±x represent the standard deviation in the PNCs during the measurement time period.

删除的内容:

	Surface Wind Speed (m/s)	T test P value	
		G_R	FLY
T1	0.5	0.2	n/a
T2	2.6	0.3	0.6
T3	5.7	2e-9	2e-7
T4	3.6	8e-5	2e-7
T5	6.7	2e-9	2e-6
T6	1.5	0.9	0.2
T7	1	0.9	0.3
T8	4.1	0.05	3e-6
T9	7.7	0.2	1e-10
T10	n/a	0.7	0.2
T11	n/a	2e-5	5e-6
T12	n/a	4e-10	1e-6
T13	n/a	0.02	1e-14
T14	n/a	0.2	1e-5

Table 2. Summary of the dates, time, wind speed, and t test results (p value) of each test flight. Wind speed values (at 1.5m) are the wind speed in the hour closest to the experiment time. From T10 to T14 the wind speed data is not available (n/a) because the instrument recording the data had broken. Flights highlighted in bold italic font indicate that the results are not significantly different at 5% significance. Flights marked in italic font indicate that the PNC on the ground with the rotor on are not significantly different from G_NR, and flights marked in standard font indicate that there are significant differences in both G_R and FLY when compared to G_NR.

	PNC RMSD (%)	
	G_R	FLY
All cases	10.2	26.2
Low wind speed cases (w<2.6m/s)	2.4	5
High wind speed cases (2.6<w<7.7m/s)	12.6	31.4
	PNC MAD (%)	
	G_R	FLY
All flights	7.8	19.1
Low wind speed cases (w<2.6m/s)	2.3	3
High wind speed cases (2.6<w<7.7m/s)	10.9	26.3

Table 3. Summary of RMSD and MAD for all cases, low wind cases, and high wind cases.

带格式的: 字体颜色: 文字 1
带格式的: 字体颜色: 文字 1
带格式的: 字体颜色: 文字 1
带格式的: 字体颜色: 文字 1
带格式的: 字体颜色: 文字 1
带格式的: 字体颜色: 文字 1
带格式的: 字体颜色: 文字 1
带格式的: 字体颜色: 文字 1
带格式的: 字体颜色: 文字 1
带格式的: 字体颜色: 文字 1
带格式的: 字体颜色: 文字 1
带格式的: 字体颜色: 文字 1
带格式的: 字体颜色: 文字 1
删除的内容: **4**

删除的内容: Summary of the dates, time, wind speed, and t test results (p value) of each test flight. Wind speed values (at 1.5m) are the wind speed in the hour closest to the experiment time. From T10 to T14 the wind speed data is not available (n/a) because the instrument recording the data had broken. Flights highlighted in green and bold italic font indicate that the results are not significantly different at 5% significance. Flights marked in yellow and italic font indicate that the PNC on the ground with the rotor on are not significantly different from G_NR, and flights marked in red and standard font indicate that there are significant differences in both G_R and FLY when compared to G_NR.

删除的内容: **5**

	Surface Wind Speed (m/s)	Sample flow rate (cm^3 /s)		
		G_NR	G_R	FLY
T1	0.5	3.04±0.04	3.03±0.04	n/a
T2	2.6	3.04±0.04	3.04±0.05	3.03±0.12
T3	5.7	3.03±0.04	3.03±0.06	3.03±0.20
T4	3.6	3.04±0.04	3.03±0.05	3.03±0.16
T5	6.7	3.02±0.04	3.02±0.04	3.00±0.26
T6	1.5	3.02±0.04	3.03±0.04	3.03±0.15
T7	1	3.03±0.03	3.03±0.05	3.03±0.17
T8	4.1	3.03±0.03	3.03±0.04	2.99±0.28
T9	7.7	3.03±0.04	3.03±0.05	3.02±0.21
T10	n/a	3.02±0.04	3.02±0.04	3.03±0.19
T11	n/a	3.02±0.04	3.02±0.04	3.03±0.22
T12	n/a	3.02±0.03	3.02±0.04	3.04±0.16
T13	n/a	3.02±0.04	3.03±0.04	3.03±0.23
T14	n/a	3.02±0.04	3.02±0.05	3.00±0.17

Table 4. Summary of the sample flow rates of each test flight at three stages. n/a = not applicable. The numbers denoted by ±x represent the standard deviation in the sample flow rates during the measurement time period.

带格式的: 字体颜色: 文字 1
带格式的: 字体颜色: 文字 1
带格式的: 字体颜色: 文字 1
带格式的: 字体颜色: 文字 1
带格式的: 字体颜色: 文字 1
带格式的: 字体颜色: 文字 1
带格式的: 字体颜色: 文字 1
带格式的: 字体颜色: 文字 1
带格式的: 字体颜色: 文字 1
带格式的: 字体颜色: 文字 1
带格式的: 字体颜色: 文字 1
带格式的: 字体颜色: 文字 1
带格式的: 字体颜色: 文字 1
删除的内容: **6**

	Mean Percentage Difference (%)			
	G_R (%)		FLY (%)	
	Accumulation	Coarse	Accumulation	Coarse
T1	-2.1	17.5	n/a	n/a
T2	5.4	1.6	-0.7	-7.0
T3	10.8	67.4	9.7	17.5
T4	13.3	6.8	15.0	38.3
T5	7.7	19.5	6.4	35.6
T6	-0.8	22.0	-3.6	61.8
T7	-0.3	7.5	3.3	17.2
T8	11.6	83.0	53.2	123.1
T9	4.2	0.9	15.6	48.0
T10	4.9	19.8	14.9	42.4
T11	18.0	23.8	16.8	33.9
T12	25.2	23.0	43.2	14.8
T13	4.2	18.4	13.9	55.5
T14	-5.1	4.5	7.3	29.9

	RMSD (%)			
	G_R		FLY	
	Accumulation	Coarse	Accumulation	Coarse
All cases	10.6	32.2	21.6	49.5
Low wind speed cases (w<2.6m/s)	3.4	15.8	7.8	38.6
High wind speed cases (2.6<w<7.7m/s)	12.9	38.5	25.4	53.6

	MAD (%)			
	G_R		FLY	
	Accumulation	Coarse	Accumulation	Coarse
All cases	8.1	22.6	15.7	40.4
Low wind speed cases (w<2.6m/s)	2.7	13.7	5.6	32.1
High wind speed cases (2.6<w<7.7m/s)	11.1	27.5	20.1	44.1

Table 5. Summary of mean percentage differences of size distribution between G_NR and G_R, and G_NR and FLY of each flight. The size distributions are separated into two modes: accumulation mode ($0.1 \leq d \leq 1\mu m$) and coarse mode ($d > 1\mu m$).

带格式的: 字体颜色: 文字 1
带格式的: 字体颜色: 文字 1
带格式的: 字体颜色: 文字 1
带格式的: 字体颜色: 文字 1
带格式的: 字体颜色: 文字 1
带格式的: 字体颜色: 文字 1
带格式的: 字体颜色: 文字 1
带格式的: 字体颜色: 文字 1
带格式的: 字体颜色: 文字 1
带格式的: 字体颜色: 文字 1
带格式的: 字体颜色: 文字 1
带格式的: 字体颜色: 文字 1
带格式的: 字体颜色: 文字 1
带格式的: 字体颜色: 文字 1
删除的内容: 7

	Mean PNCs (cm^{-3})	
	Up	Down
T10	1189±107	1201±101
T12	55±11	54±12
T13	72±15	82±13

Table 6. Mean PNC with standard deviations on the way up and down in three vertical profile runs.

删除的内容: **8**

Parameter	Symbol	Approx. value
Focal length of mirror	fm	10mm
Distance from mirror to image	Id	33.3mm
Distance from beam to mirror	d	14.8m
Radius of mirror	Mr	12.5mm
Distance from beam to top of mirror	h	9.77mm

Table A1. Parameters derived from information in Gao et al. 2016

带格式的: 居中

第 35 页: [1] 删除的内容　　刘 子夏　　2021/7/8 AM11:20:00